PAPER

Promoting oxygen reduction reaction kinetics through manipulating electron redistribution in CoP/Cu₃P@NC for aqueous/flexible Zn–air batteries†

Lixia Wang,[a] Jiasui Huang,[a] Jia Huang,[a] Bowen Yao,[a] Aling Zhou,[a] Zhiyang Huang,[a] Tayirjan Taylor Isimjan,*[c] Bao Wang [iD] *[b] and Xiulin Yang [iD] *[a]

Zinc–air batteries (ZABs) are considered a promising energy storage technology due to their high energy density and environmental friendliness. However, the development of efficient and durable oxygen reduction reaction (ORR) catalysts remains a challenge. Herein, we report the synthesis of a highly efficient CoP/Cu₃P@NC catalyst using a Zn-MOF template, which was transformed into N- and C-doped bimetallic phosphides via high-temperature phosphating. The CoP/Cu₃P@NC-based ZAB exhibits remarkable performance with an open-circuit voltage of 1.50 V, a peak power density of 215 mW cm^{-2}, and a specific capacity of 691 mA h g$_{zn}$$^{-1}$, outperforming conventional Pt/C-based ZABs. The catalyst maintained 93.5% of its initial activity after 300 h of cycling, demonstrating its excellent long-term stability. Furthermore, CoP/Cu₃P@NC was applied in flexible ZABs, achieving a power density of 74 mW cm^{-2} and showing stable performance under various bending conditions. The superior performance is attributed to the synergistic effects of Co and Cu, optimized structural properties, and high porosity, enhancing mass transfer and oxygen activation. These results suggest that CoP/Cu₃P@NC is a highly promising ORR catalyst for next-generation ZABs, offering both high efficiency and durability in flexible and conventional energy storage applications.

Green foundation

1. A highly efficient CoP/Cu₃P@NC catalyst was synthesized using a Zn-MOF template and high-temperature phosphating, creating N- and C-doped bimetallic phosphides for oxygen reduction reaction (ORR).

2. The CoP/Cu₃P@NC-based ZAB shows an open-circuit voltage of 1.50 V, a peak power density of 215 mW cm^{-2}, and a specific capacity of 691 mA h g$_{zn}$$^{-1}$, surpassing the conventional Pt/C-based ZAB. Moreover, it maintains 93.5% of its initial activity after 300 h of cycling and performs stably in flexible ZABs under various bending conditions.

3. The excellent performance of CoP/Cu₃P@NC is due to the synergistic effects of Co and Cu, optimized structural properties, and high porosity, making it a highly promising ORR catalyst for advancing energy conversion and storage.

[a]Guangxi Key Laboratory of Low Carbon Energy Materials, School of Chemistry and Pharmaceutical Sciences, Guangxi Normal University, Guilin 541004, China.
E-mail: xlyang@gxnu.edu.cn
[b]State Key Laboratory of Biochemical Engineering, Institute of Process Engineering, Chinese Academy of Sciences, Beijing 100190, China. E-mail: baowang@ipe.ac.cn
[c]Saudi Arabia Basic Industries Corporation (SABIC) at King Abdullah University of Science and Technology (KAUST), Thuwal 23955-6900, Saudi Arabia.
E-mail: isimjant@sabic.com
†Electronic supplementary information (ESI) available. See DOI: https://doi.org/10.1039/d4gc05538a

1. Introduction

Zinc–air batteries (ZABs) offer significant potential in energy conversion and storage technologies, due to their high energy density, affordability, and cleanliness.[1,2] Unfortunately, the exorbitant cost of precious metals (such as Pt), limited reserves, and inadequate long-term stability pose major challenges to their widespread adoption.[3,4] Rok Stropnik's team highlighted that just 0.75 g of Pt accounts for approximately 60% of the environmental impact in manufacturing a 1 kW polymer electrolyte membrane fuel cell (PEMFC) system.[5] Similarly, Shoki Kosai et al. reported that Pt production gener-

ates approximately 10 000 kg CO_2-eq per kg in terms of global warming potential (GWP).[6] Consequently, Pt's high cost and significant environmental impact underscore the importance of reducing its usage and exploring non-precious metal catalysts as alternatives.[7] The cathodic oxygen reduction reaction (ORR) in ZABs takes place at the gas–solid–liquid three-phase interface.[8] Specifically, reactive oxygen molecules adsorb onto the active sites of the electrocatalyst, leading to the formation of reaction intermediates and enabling multiple electron transfer steps that complete the ORR process.[9] During this process, the catalytic site activity, electron transfer capability of the catalyst, and the stability of the three-phase interface are critical factors affecting the ORR rate.[10] To surmount these challenges, it is imperative to explore well-designed materials with high porosity, efficient utilization of active sites, and excellent electrical conductivity to improve mass transfer and enhance the ORR performance in ZABs.[11]

Metal–organic frameworks (MOFs) have been widely employed as self-templated precursors for transition metal-doped carbon composites due to their high porosity, versatility, and organic metal-site linkages.[12] The porous carbon framework formed from the *in situ* transformation of MOF-derived materials through high-temperature carbonization typically exhibits high electrical conductivity while maintaining a porous structure, enhancing the stability of the active centers and reducing the charge transfer energy barrier of the parent MOF.[13,14] Incorporating heteroatoms into carbon materials can disrupt their electroneutrality and modify charge density distribution, thus improving the ORR performance.[15] Additionally, nitrogen heteroatoms can form chemical bonds with transition metal atoms, increasing their stability on the carbon substrate.[16] A diverse range of MOF derivatives, including porous carbon materials,[17,18] metal/metal oxides,[19,20] sulfides,[21,22] nitrides,[23,24] and phosphides,[25,26] have garnered attention for their high performance and affordability.[27,28] In virtue of the abundant active sites, tunable structural components, and plentiful resources of transition metal phosphides, they are emerging as promising candidates for oxygen catalysts.[29] Undeniably, the catalytic activity of single-component catalysts is often inadequate.[30] The rational design of two-component catalysts can not only regulate the electronic structure and optimize adsorption behavior, but also enhance the intrinsic activity of the catalyst. By carefully selecting and combining two distinct components, it is possible to create synergistic effects and improve the overall catalytic performance.[31] Moreover, the design can be adapted to specific reaction conditions, further optimizing the catalyst's functionality.[32] For instance, Guo *et al.* reported that Fe_2P-Co_2P/NPC demonstrated excellent ORR activity with a half-wave potential of 0.95 V, outperforming pure Co_2P@NPC and Fe_2P@NPC. Density functional theory (DFT) results signified that the catalyst exhibited optimal adsorption free energies, projected density of states (PDOS), and *d*-band centers.[33] As a result, integrating dual transition metal phosphides with N-doped carbon supports is anticipated to significantly enhance both conductivity and ORR activity.[34]

In light of these considerations, we successfully synthesized cake-like CoP/Cu_3P@NC composites with a fluffy porous structure using Zn-MOFs as a self-template, surface-coated with bimetallic CoCu species, and a high-temperature gas-phase phosphating method. This porous structure significantly increases the specific surface area and porosity, facilitating effective mass and charge transport, and ultimately improving the ORR performance. The optimized CoP/Cu_3P@NC showed impressive ORR activity, fast reaction kinetics, and satisfactory stability in an alkaline solution. Even more promisingly, CoP/Cu_3P@NC-based liquid/flexible ZABs exhibited high power densities of 215 and 74 mW cm^{-2}, outperforming most recently reported catalyst-assembled ZABs.

2. Experimental section

2.1. Materials

Cobalt(II) nitrate hexahydrate ($Co(NO_3)_2 \cdot 6H_2O$, 99%), zinc acetate dihydrate ($Zn(Ac)_2$, 99.0%), ammonia ($NH_3 \cdot H_2O$, 25–28%) and potassium hydroxide (KOH, 99.0%) were sourced from Guangxi Zoey Biotechnology Co., Ltd. Poly(vinylpyrrolidone) ((C_6H_9NO)n, 99%, PVP), benzimidazole ($C_7H_6N_2$, 98%), and dopamine hydrochloride ($C_8H_{11}NO_2 \cdot HCl$, 98%) were obtained from Aladdin Industrial Corporation. Red phosphorus (P, 98.5%), Nafion solution (5 wt%), and commercial Pt/C (20 wt% platinum) were acquired from Alfa Aesar. Copper acetate trihydrate ($Cu(NO_3)_2 \cdot 3H_2O$, 99%) and zinc nitrate hexahydrate ($Zn(NO_3)_2 \cdot 6H_2O$, 99.0%) were purchased from Sinopharm Chemical Reagent Co., Ltd. Methanol (AR, 99.5%) and ethanol absolute (C_2H_5OH, 99.7%) was obtained from Xilong Chemical Co., Ltd. Ruthenium chloride ($RuCl_3 \cdot xH_2O$, 99.95%) was sourced from Innochem, and RuO_2 powder was produced by calcining $RuCl_3$ in air at 400 °C.

2.2. Synthesis of the Zn-MOF precursor

The Zn-MOF precursor was synthesized *via* a room temperature stirring reaction, following the procedure described in our previous report.[35]

2.3. Synthesis of CoCuZn-PDA

Initially, 300 mg of Zn-MOFs were dispersed in 30 mL of deionized water. Then, 0.3 g of dopamine hydrochloride was added under ultrasonic conditions. The pH of the solution was meticulously adjusted to 9.0 by incrementally adding ammonia. Subsequently, 1 mmol each of cobalt nitrate and copper nitrate were incorporated into the mixture, which was agitated at room temperature for 12 h. The resulting solution was washed with deionized water and ethanol, followed by centrifugation and drying, yielding CoCuZn-PDA.

2.4. Synthesis of CoP/Cu_3P@NC, CoP@NC and Cu_3P@NC

The CoCuZn-PDA samples were mixed with red phosphorus at a 1 : 2 ratio. The mixture was then heated to 900 °C (or alternatively at 800/1000/1100 °C) under a N_2 atmosphere with a

heating rate of 2 °C min^{-1}, and maintained for 2 h to obtain CoP/Cu$_3$P@NC.

To optimize the Co and Cu content in the bimetallic phosphides, samples were synthesized with cobalt nitrate/copper nitrate molar ratios of 0.5 : 1.5 and 1.5 : 0.5, while keeping the total molar amount of metal salts constant at 2 mmol. These samples were designated as Co$_{0.5}$Cu$_{1.5}$P@NC and Co$_{1.5}$Cu$_{0.5}$P@NC, respectively. Moreover, single contrast samples CoP@NC and Cu$_3$P@NC were synthesized using the same protocol, but without the addition of copper nitrate or cobalt nitrate, respectively.

2.5. Synthesis of CoCu@NC and P@NC

For comparison, the CoCuZn-PDA precursor was calcined under a N$_2$ atmosphere without phosphatization to obtain Co/Cu@NC. Meanwhile, Zn-MOFs-PDA underwent phosphatization without any metal addition, resulting in the production of P@NC.

3. Results and discussion

3.1. Synthesis and structural analysis of catalysts

Fig. 1a illustrates the synthesis route for the elaborately fabricated CoP/Cu$_3$P@NC. Briefly, numerous discoidal Zn-MOFs were self-assembled by introducing a solution containing Zn^{2+} into a benzimidazole solution. These Zn-MOFs served as self-templates for the subsequent synthesis, providing a favorable framework for the growth and dispersion of active species. Next, the metal cations Co^{2+} and Cu^{2+} were encapsulated in the outer layer of Zn-MOFs, utilizing the multifunctional coating effect of dopamine hydrochloride.[36,37] N- and C-doped (NC) bimetallic phosphides CoP/Cu$_3$P@NC were synthesized

via a high-temperature phosphating strategy under an inert atmosphere, in which porous NC was derived from self-templated Zn-MOFs.[38] The X-ray diffraction (XRD) pattern reveals that the crystalline phase of Zn-MOFs is consistent with the previous reports (Fig. S2†).[35] The CoCuZn-PDA precursor existed predominantly as a metal oxide/hydroxide before phosphorylation (Fig. S3†). The XRD patterns of the synthesized catalysts (Fig. 1b† and Fig. S4†) exhibit diffraction peaks corresponding to CoP (JCPDS: 29-0497) and Cu$_3$P (JCPDS: 02-1263). Importantly, no impurity peaks were detected in the XRD spectra, apart from the C peak located at 20°,[39] indicating the absence of an impurity phase. The Raman spectra disclose that all the prepared catalysts exhibit prominent peaks at 1358 cm^{-1} and 1595 cm^{-1}, corresponding to the D and G bands, respectively.[40] The D band indicates structural defects in the carbon lattice caused by nitrogen atoms, while the G band corresponds to the sp^2 hybridized graphitic carbon structure. The I_D and I_G values were determined from the peak height,[41] and the I_D/I_G ratio of the catalysts increased as the phosphating temperature increased from 800 °C to 1100 °C (Fig. S5†), indicating a higher defect density and reduced electrical conductivity. Compared to CoP@NC and (0.87) Cu$_3$P@NC (0.62), the CoP/Cu$_3$P@NC catalyst exhibited an intermediate I_D/I_G value of 0.70, indicating a balanced ratio of defects and conductivity (Fig. 1c).[42] This balance facilitates optimal intermediate adsorption, thereby enhancing catalytic performance.[43,44] The contact angles of CoP/Cu$_3$P@NC, CoP@NC, and Cu$_3$P@NC were measured at 44.5°, 39.2°, and 51.6°, respectively, showing that Cu$_3$P@NC exhibits weaker hydrophilicity. The incorporation of CoP@NC enhanced hydrophilicity, which facilitates the adsorption of OH$^-$ (Fig. 1d).[45]

The morphology and structure of the synthesized samples were analyzed using scanning electron microscopy (SEM) and
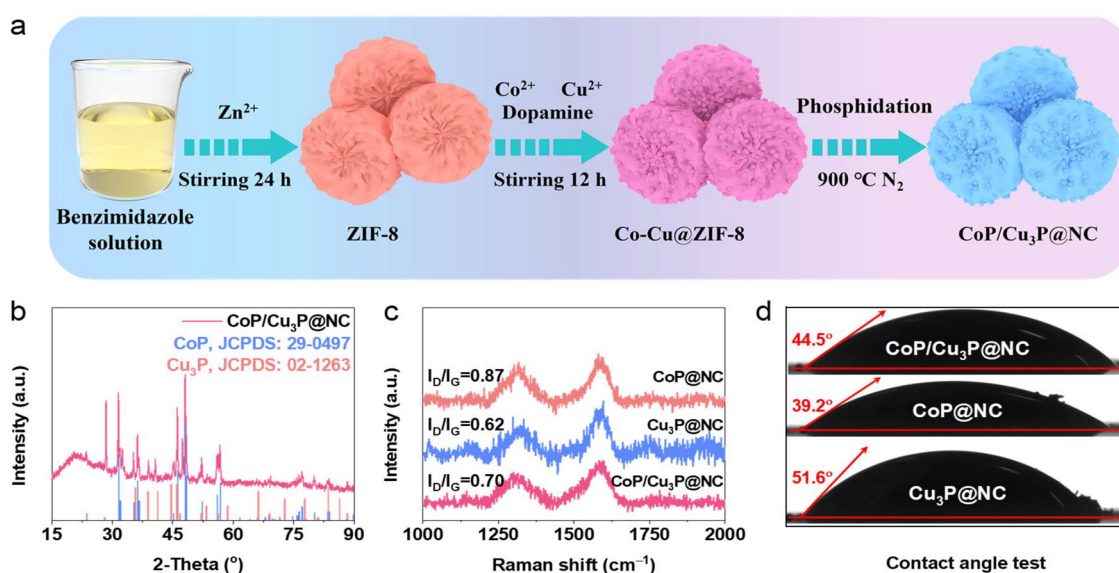

Fig. 1 (a) Schematic illustration of the synthesis process. (b) XRD pattern of CoP/Cu$_3$P@NC. (c) Raman spectra of CoP@NC, Cu$_3$P@NC, and CoP/Cu$_3$P@NC. (d) Contact angle measurements of CoP/Cu$_3$P@NC, CoP@NC, and Cu$_3$P@NC.

transmission electron microscopy (TEM). The results clearly validated that the CoCuZn-PDA precursor retained the cake-like structure of Zn-MOFs, though its surface exhibited increased roughness (Fig. 2a). After high-temperature phosphatization, $CoP/Cu_3P@NC$ well inherited the overall cake-like morphology with prominent nanoparticles appearing on its surface (Fig. 2b), as further confirmed by TEM analysis (Fig. 2c). High-resolution transmission electron microscopy (HR-TEM) images indisputably show that the crystal plane spacing of $CoP/Cu_3P@NC$ is 0.196 nm, corresponding to the (112) mirror of CoP. The spacings of 0.210, 0.201, and 0.199 correspond to the (003), (300), and (113) crystal planes of Cu_3P, respectively (Fig. 2d). Furthermore, the selected area electron diffraction (SAED) pattern (Fig. 2e) confirmed the presence of both CoP and Cu_3P, in agreement with the XRD results. Elemental mapping further revealed that in $CoP/Cu_3P@NC$, Co and P are concentrated in nanoparticles, while Cu, C, and N are uniformly distributed throughout the structure (Fig. 2g). This manifests that during the phosphating process, the solid Co and Cu species embedded in the N-doped carbon matrix were converted into CoP nanoparticles, with uniformly dispersed Cu_3P formed *via* the Kirkendall effect.[16,46] This effect plays a crucial role in enabling atomic diffusion and the formation of new phases during the transition.

The surface elemental bonding information of the synthesized catalysts was investigated using X-ray photoelectron spectroscopy (XPS). The XPS survey spectrum (Fig. S6†) of $CoP/Cu_3P@NC$ confirms the presence of Co, Cu, P, C, N, and O signals, with elemental O likely resulting from unavoidable surface oxidation. The high-resolution C 1s spectrum (Fig. S7†) of $CoP/Cu_3P@NC$ can be resolved into four peaks attributed to C=C (284.0 eV), C–C (284.7 eV), C–O (286.0 eV) and C=O (288.9 eV), respectively.[44] The high-resolution Co 2p spectra exhibit three doublet peaks assigned to the Co–P, Co–O, and satellite peaks (Fig. 3a). Notably, the binding energy of the Co–P peak for $CoP/Cu_3P@NC$ exhibits a negative shift of approximately 0.32 eV compared to that of CoP@NC, indicating that CoP functions as an electron acceptor in $CoP/Cu_3P@NC$.[47] Deconvolution of the high-resolution Cu 2p spectra (Fig. 3b) identifies peaks corresponding to Cu^+ (933.2 eV), Cu^{2+} (935.5 eV), and associated satellite peaks (934.4 eV).[48] Furthermore, the Auger electron spectrum of Cu LMM illustrates a peak at 569.6 eV, further confirming the presence of Cu^+ (Fig. S8†). Similarly, $CoP/Cu_3P@NC$ exhibits a positive shift of 0.23 eV for the Cu^+ peak compared to $Cu_3P@NC$, highlighting the electron donor properties of the Cu_3P site in $CoP/Cu_3P@NC$. This observation indicates that electron transfer from Cu_3P to CoP leads to electron redistribution within the CoP/Cu_3P structure. As depicted in Fig. 3c, the P 2p spectra of $CoP/Cu_3P@NC$ exhibit three distinct peaks attributed to P–O_x (132.6 eV), Co–P $2p_{1/2}$ (130.0 eV), and Co–P $2p_{3/2}$ (129.3 eV), verifying the presence of M–P bonding.[46] The XPS content (%) of the different elements in the synthesized catalysts and the proportions of each component are summarized in Tables S1 and S2.† As illustrated in Fig. 3d, the high-resolution N 1s spectra of all samples reveal the presence of pyridinic-N (398.1 eV), pyrrolic-N (400.2 eV), graphitic-N (401.3 eV), and oxidic-N (403.4 eV) species.[49] The significant abundance of pyridine N in the sub-
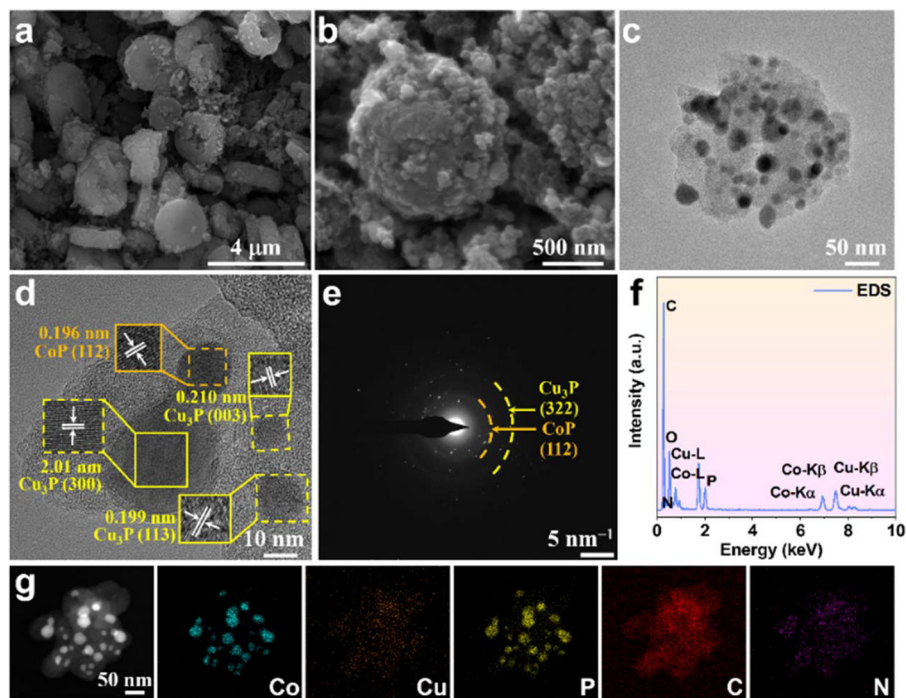

Fig. 2 (a) SEM image of the CoCuZn-PDA precursor. (b) SEM image, (c) TEM image, (d) HR-TEM image, (e) SAED pattern, (f) EDS pattern, and (g) HAADF-STEM images and the corresponding elemental mappings of $CoP/Cu_3P@NC$.
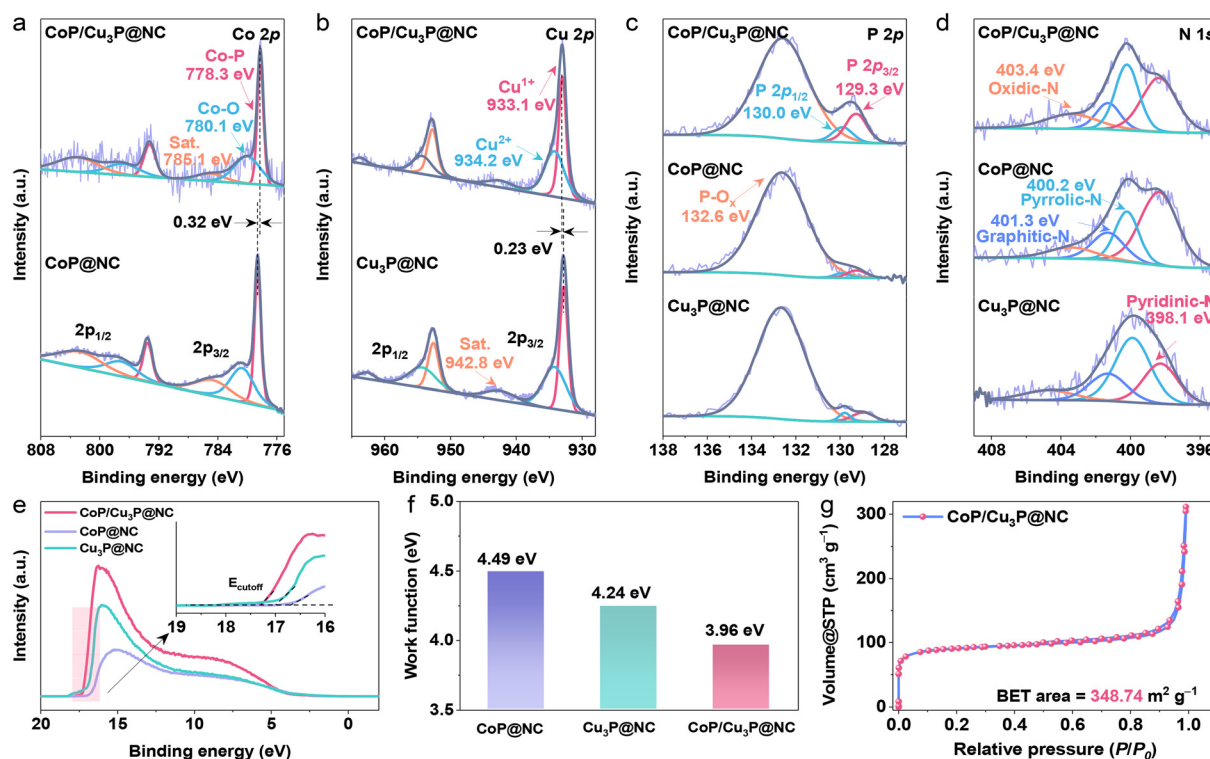
Fig. 3 High-resolution XPS spectra of (a) Co 2p, (b) Cu 2p, (c) P 2p, and (d) N 1s in as-synthesized samples. (e) UPS spectra with inset partial enlargement of CoP/Cu₃P@NC, CoP@NC and Cu₃P@NC catalysts and (f) corresponding work function. (g) N₂ adsorption−desorption isotherm of CoP/Cu₃P@NC.

strate material NC provides ample anchoring sites for metal phosphides (Table S3†).[50] Ultraviolet photoelectron spectroscopy (UPS) measurements of the work function (WF) were conducted to elucidate the surface electronic properties and the valence band structures of the catalysts (Fig. 3e).[51,52] The WFs for CoP@NC, Cu₃P@NC, and CoP/Cu₃P@NC are 4.49, 4.24, and 3.96 eV, respectively (Fig. 3f), indicating that CoP/Cu₃P@NC is closer to the Fermi level than both CoP@NC and Cu₃P@NC. The differences in WFs among these catalysts confirm that electron transfer from higher to lower energy levels promotes charge redistribution.[53] This finding further supports that electron transfer occurs from Cu₃P to CoP at the interface, consistent with the XPS results. Notably, CoP/Cu₃P@NC exhibits the lowest WF, indicating a shift of its d-band center towards the Fermi energy level. This suggests that valence electrons predominantly arise from the d state,[52,54] providing evidence for the efficient activation of molecular oxygen and enhancing the ORR activity.[55] Moreover, N₂ adsorption/desorption was conducted to investigate the porous structure, pore distribution, and surface area of the sample. As indicated in Fig. 3g, the CoP/Cu₃P@NC catalyst exhibits a high Brunauer–Emmett–Teller (BET) specific surface area (348.74 m² g⁻¹). The sample also demonstrates mesoporous features with a pore size of 6.43 nm, as observed from the plot (Fig. S9†). The high specific surface area and distinctive mesoporous structure facilitate widespread exposure of active sites and comprehensive contact with reactive species.[56]

3.2. ORR activity in alkaline media

The ORR activity of the catalysts was evaluated using linear scanning voltammetry (LSV) with rotating disk electrode (RDE) and rotating ring disk electrode (RRDE) techniques in an oxygen/nitrogen-saturated 0.1 M KOH electrolyte. Optimization of the catalyst performance was achieved by adjusting the molar ratios of Co/Cu metal salts (Fig. S10†) and phosphating temperatures (Fig. S11†). The results revealed that CoP/Cu₃P@NC exhibited competitive advantages, with an optimal half-wave potential and limiting current density at a Co/Cu molar ratio of 1 : 1 and a phosphating temperature of 900 °C. In contrast to N₂-saturated solutions, all samples exhibited distinct cathodic peaks in the O₂-saturated electrolyte, indicating a more efficient ORR process. The cyclic voltammetry (CV) curves for CoP/Cu₃P@NC showed a dominant oxygen reduction peak compared to CoP@NC, Cu₃P@NC, and Pt/C, underscoring its superior ORR catalytic activity (Fig. 4a). As depicted in Fig. 4b and Fig. S12,† CoP/Cu₃P@NC showcased a higher limiting current density compared to their single-metal counterparts, CoCu@NC and P@NC, highlighting the enhanced ORR activity due to the Co/Cu bimetallic phosphides. In the 0.2–0.8 V range, the ring currents for Cu₃P@NC, CoP@NC, CoP/Cu₃P@NC, and Pt/C are approximately 0.17, 0.30, 0.25, and 0 mA cm⁻², respectively. This indicates that the introduction of Cu₃P effectively reduces the H₂O₂ yield of CoP. In addition, the onset potential (E_{onset}, the potential at 0.1 mA
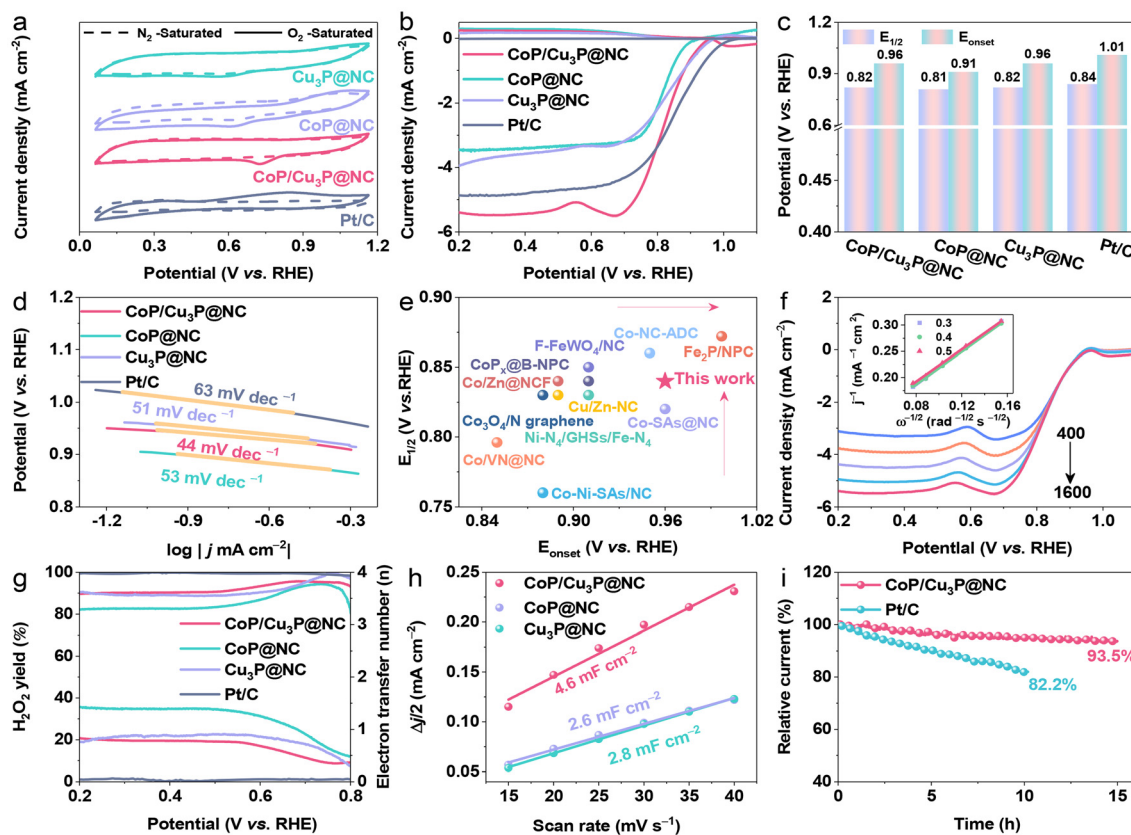
Fig. 4 Electrochemical performance of different catalysts. (a) CV curves in N_2 or O_2-saturated 0.1 M KOH solution. (b) LSV polarization curves in O_2-saturated 0.1 M KOH electrolyte, and (c) the corresponding half-wave potential ($E_{1/2}$) and onset potential (E_{onset}), (d) Tafel plots. (e) Comparison of the ORR activity of CoP/Cu_3P@NC with recently reported materials. (f) Polarization curves of CoP/Cu_3P@NC with various rotating speeds from 400 to 1600 rpm and the corresponding K–L plots (inset). (g) H_2O_2 yield (%) and electron transfer number (n), (h) C_{dl} values for various catalysts, and (i) the corresponding stability test in O_2-saturated 0.1 M KOH solution at a rotating speed of 1600 rpm.

cm^{-2}) and half-wave potential ($E_{1/2}$) of the synthesized catalysts are summarized in Fig. 4c. The ORR kinetics were analyzed using Tafel curves (Fig. 4d), which revealed that CoP/Cu_3P@NC exhibited a Tafel slope of 44 mV dec^{-1}. This value is lower than those of CoP@NC (53 mV dec^{-1}), Cu_3P@NC (51 mV dec^{-1}), and Pt/C (63 mV dec^{-1}), indicating that CoP/Cu_3P@NC possesses more favorable ORR kinetics.[57] Electrochemical impedance spectroscopy (EIS) demonstrated that CoP/Cu_3P@NC exhibited lower charge transfer resistance (Fig. S13†), validating that the synergistic coupling between CoP and Cu_3P accelerates the charge transfer process.[58] To further validate the catalysts' conductivity, a four-point probe was used to measure resistivity and conductivity (Table S4†). CoP/Cu_3P@NC exhibited a resistance of 39.8 Ω, which is significantly lower than that of CoP@NC (47.0 Ω) and Cu_3P@NC (51.1 Ω). Additionally, its conductivity was measured at 25.13 S cm^{-1}, notably higher than CoP@NC (21.28 S cm^{-1}) and Cu_3P@NC (19.57 S cm^{-1}). These findings are consistent with the results of the prior EIS analysis. Notably, CoP/Cu_3P@NC outperformed Pt/C and many of the previously reported catalysts (Fig. 4e and Table S5†). The LSV curves of CoP/Cu_3P@NC at varying rotation speeds (400 to 1600 rpm) are illustrated in

Fig. 4f. The electron transfer number (n) during the ORR process was determined to be close to 4, within the range of 0.3–0.5 V, as verified using Koutecky–Levich (K–L) plots (inset in Fig. 4f). RRDE measurements (Fig. 4g) further evaluated the hydrogen peroxide yield and electron transfer number, showing the lowest H_2O_2 yield and an electron transfer number near 4, confirming oxygen reduction via a direct four-electron pathway. This suggests that the electronic interaction between Co and Cu sites in the bimetallic phosphide augments the intrinsic activity of CoP/Cu_3P@NC sites. Constructing porous structures provides diffusion channels, increasing the contact area between the catalyst and electrolyte, improving mass transfer, and reducing diffusion limitations. To gain further insight, the electrochemical double-layer capacitance (C_{dl}) was calculated from the non-faradaic region of CV curves at different scan rates (Fig. S14†). Since C_{dl} is positively correlated with the electrochemically active surface area (ECSA), it serves as an indicator of the active surface area of catalysts. CoP/Cu_3P@NC exhibited a higher C_{dl} value of 4.6 mF cm^{-2}, compared to CoP@NC (2.6 mF cm^{-2}) and Cu_3P@NC (2.8 mF cm^{-2}) (Fig. 4h), indicating a larger ECSA and more exposed active sites, thereby enhancing cata-

lytic activity. The stability of CoP/Cu$_3$P@NC was evaluated using chronoamperometry in an O$_2$-saturated 0.1 M KOH electrolyte. CoP/Cu$_3$P@NC showed minimal current fluctuation and retained 93.5% of its initial activity after 15 h, whereas commercial Pt/C retained only 82.2% after 10 h (Fig. 4i). The superior stability of CoP/Cu$_3$P@NC compared to Pt/C is attributed to the strong synergistic interaction between Co/Cu bimetallic phosphides. Additionally, nitrogen-doped carbon supports play a crucial role in redistributing charge at the active sites, preventing nanoparticle migration and aggregation during the ORR process, thereby significantly enhancing the long-term durability of CoP/Cu$_3$P@NC. SEM, TEM, and XPS analyses (Fig. S15–S17†) revealed that the catalysts maintained their fluffy structure after the long-term stability test, with elemental mapping closely resembling the initial state. XPS results showed a slight increase in high valence metal content post-testing, which may be crucial in further enhancing ORR activity.[59] Overall, CoP/Cu$_3$P@NC exhibited remarkable compositional and structural stability.

3.2.   Test for performance of the assembled ZABs

To demonstrate the viability of CoP/Cu$_3$P@NC in battery devices, we constructed liquid flow zinc–air batteries (ZABs) using CoP/Cu$_3$P@NC as the air cathode, zinc foil as the anode, and a 6.0 M KOH electrolyte solution containing 0.2 M Zn(CH$_3$COO)$_2$ (Fig. 5a). For comparison, Pt/C-based ZABs were also fabricated. As depicted in Fig. 5b, the open-circuit voltage of CoP/Cu$_3$P@NC is 1.50 V, slightly higher than Pt/C (1.42 V). As illustrated in Fig. 5c, CoP/Cu$_3$P@NC achieves a peak power density of 215 mW cm^{-2}, which is significantly higher than Pt/C (129 mW cm^{-2}) and most recently reported phosphide catalysts (Table S6†). In terms of specific capacity (Fig. 5d), CoP/Cu$_3$P@NC-based ZABs reach 691 mA h g$_{zn}^{-1}$, comparable to Pt/C (698 mA h g$_{zn}^{-1}$). More attractively, CoP/Cu$_3$P@NC exhibits a stable discharge plateau across a wide range of current densities (2–20 mA cm^{-2}), showcasing excellent multiplicative performance (Fig. 5e). Given the suboptimal performance of CoP/Cu$_3$P@NC in the oxygen evolution reaction (OER)
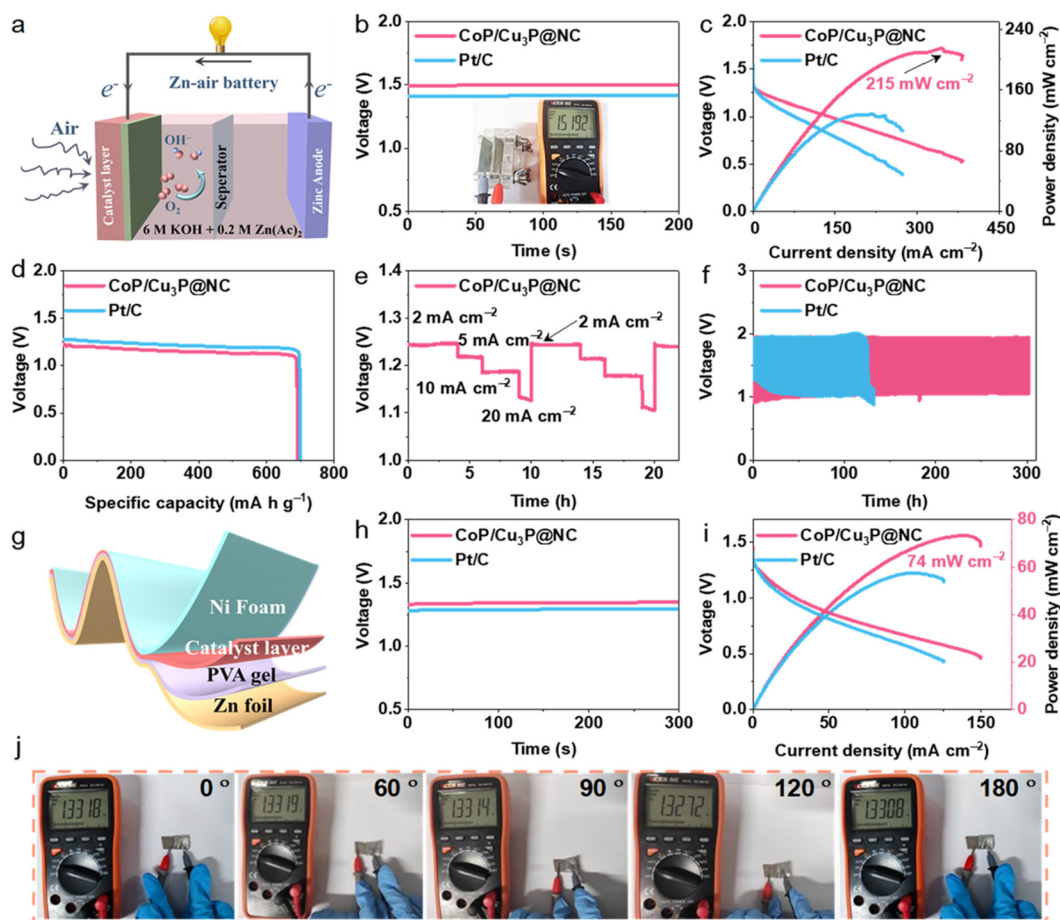

Fig. 5   (a) Schematic configuration of the assembled aqueous ZAB. (b) Open circuit voltage (OCV) plots (inset: an optical image for OCV measured using a multimeter), (c) power density, (d) specific capacity curves of liquid-state ZABs using CoP/Cu$_3$P@NC or Pt/C as the air electrode. (e) Discharge curves at various current densities. (f) Galvanostatic cycling at a current density of 5 mA cm^{-2} (20 min for each cycle). (g) Sketch diagram of the flexible ZAB. (h) OCV of CoP/Cu$_3$P@NC and Pt/C based flexible ZABs, (i) the discharge polarization and corresponding power density profiles. (j) Photographs of CoP/Cu$_3$P@NC-based flexible ZAB powered by LED panel at different bending angles (0–180°).

(467 mV@10 mA cm^{-2}, Fig. S18†), we assessed the long-term cycling stability of electrochemical charge/discharge in a CoP/Cu$_3$P@NC + RuO$_2$-based ZAB system (Fig. 5f). The CoP/Cu$_3$P@NC battery demonstrated stable performance, maintaining its efficiency even after 300 h of cycling. In contrast, the ZAB with a Pt/C + RuO$_2$ air cathode exhibited rapid performance degradation after only 128 h, accompanied by limited charging capacity. The development of solid-state ZABs is crucial for flexible electronic energy devices. We constructed a highly adaptable solid-state ZAB using commercial zinc foil as the anode and a PAV hydrogel saturated with KOH-Zn (CH$_3$COO)$_2$ as the quasi-solid electrolyte, leveraging CoP/Cu$_3$P@NC as the air cathode (Fig. 5g). As anticipated in Fig. 5h, the OCV of the CoP/Cu$_3$P@NC-based solid-state ZAB (1.35 V) surpassed that of Pt/C (1.31 V) and other Co/Cu-based flexible devices (Table S7†). The discharge polarization curves (Fig. 5i) reveal that the CoP/Cu$_3$P@NC-based ZAB achieved a power density of 74 mW cm^{-2}, higher than the solid-state ZAB with a Pt/C air cathode (57 mW cm^{-2}). Moreover, the CoP/Cu$_3$P@NC cathode maintained a nearly constant voltage under bending at 0°, 60°, 90°, 120°, and 180° (Fig. 5j), demonstrating admirable mechanical flexibility and stability, which are crucial for flexible electronic applications.

The remarkable ORR catalytic activity and outstanding durability of CoP/Cu$_3$P@NC can be ascribed to the synergistic composition and architectural advantages derived from several key aspects: (i) the balance between graphitization and carbon defects enhances conductivity and corrosion resistance, inhibits metal phosphide agglomeration, and improves catalyst stability; (ii) the fluffy, cake-like structure improves the contact between the electrode and electrolyte, facilitating the rapid transfer of reactants, intermediates, and products, as well as the transport of electrolyte ions; (iii) the variation in WFs between the catalysts promotes charge redistribution, shifts the d-band center toward the Fermi energy level, and effectively activates oxygen molecules; (iv) the porosity generated by the pyrolytic evaporation of zinc from the Zn-MOFs ensures the sufficient availability of active sites, enabling the elevated electrocatalytic ORR performance.

4. Conclusion

The CoP/Cu$_3$P@NC catalyst demonstrates superior ORR performance and durability, making it a promising candidate for both liquid and solid-state zinc–air batteries (ZABs). Key performance metrics, including the open-circuit voltage (OCV) of 1.50 V, the peak power density of 215 mW cm^{-2}, and the specific capacity of 691 mA h g$_{zn}^{-1}$, all significantly surpass those of the conventional Pt/C-based systems. Moreover, the catalyst maintained stable discharge performance over extended cycles, retaining 93.5% of its capacity after 300 h, far exceeding the Pt/C-based ZABs that degraded after only 128 h. In solid-state ZABs, the CoP/Cu$_3$P@NC air cathode continued to show superior power density (74 mW cm^{-2}) and flexibility, maintaining consistent performance even under mechanical

bending at various angles (0° to 180°), highlighting its potential for flexible electronic applications. The performance advantages of CoP/Cu$_3$P@NC stem from several synergistic effects, including the optimized balance between conductivity and defect density, enhanced electrode–electrolyte interactions, and improved oxygen activation, all driven by the unique bimetallic phosphide structure and high porosity. These results demonstrate that CoP/Cu$_3$P@NC possesses remarkable ORR catalytic activity, presenting a promising avenue for advancing energy conversion and storage technologies.

Author contributions

Lixia Wang: investigation, conceptualization, and writing – original draft. Jiasui Huang: investigation. Jia Huang: data curation. Bowen Yao: methodology. Aling Zhou: data curation. Zhiyang Huang: methodology. Tayirjan Taylor Isimjan: writing – review & editing. Bao Wang: writing – review & editing. Xiulin Yang: supervision and writing – review & editing.

Data availability

Data for this article, including compound characterization, calculations, and experimental data, are available as the ESI† at **https://doi.org/10.1039/D4GC05538A**.

Conflicts of interest

There are no conflicts to declare.

Acknowledgements

References

1 L. Gao, X. Zhong, Z. Li, J. Hu, S. Cui, X. Wang and B. Xu, *Chem. Commun.*, 2024, **60**, 1269–1272.

2 H. Wang, L. Kang, K. Wang, M. Wei, P. Pei, Y. Zuo and B. Liang, *Adv. Funct. Mater.*, 2024, **34**, 2407347.

3 T. Qin, Z. Pei, J. Qiu, J. Wang, Z. Xu and X. Guo, *Small*, 2024, **20**, 2402762.

4 L. Wu, Y. Chen, C. Shao, L. Wang and B. Li, *Adv. Funct. Mater.*, 2024, **34**, 2408257.

5 R. Stropnik, A. Lotrič, A. B. Montenegro, M. Sekavčnik and M. Mori, *Energy Sci. Eng.*, 2019, **7**, 2519–2539.

6 S. Kosai and E. Yamasue, *Sci. Total Environ.*, 2019, **651**, 1764–1775.

7 A. Pedersen, J. Pandya, G. Leonzio, A. Serov, A. Bernardi, I. E. L. Stephens, M.-M. Titirici, C. Petit and B. Chachuat, *Green Chem.*, 2023, **25**, 10458–10471.

8 Q. Liu, L. Wang and H. Fu, *J. Mater. Chem. A*, 2023, **11**, 4400–4427.

9 Y. Wu, J. Sun, S. Dou and J. Sun, *J. Energy Chem.*, 2022, **69**, 54–69.

10 H. Jiang, R. Luo, Y. Li and W. Chen, *EcoMat*, 2022, **4**, e12199.

11 M. Perumalsamy, A. Sathyaseelan, S. Kamalakannan, V. Elumalai, H. C. Ham and S.-J. Kim, *Energy Storage Mater.*, 2024, **70**, 103447.

12 Z. He, R. Sun, H. Xu, W. Geng and P. Liu, *Carbon*, 2024, **219**, 118853.

13 W. Wang, H. Yan, U. Anand and U. Mirsaidov, *J. Am. Chem. Soc.*, 2021, **143**, 1854–1862.

14 J. Sun, W. Gao, H. Fei and G. Zhao, *Appl. Catal., B*, 2022, **301**, 120829.

15 Y. Huang, F. Kong, F. Pei, L. Wang, X. Cui and J. Shi, *EcoMat*, 2023, **5**, e12335.

16 W. Zhu, W. Hu, Y. Wei, Y. Zhang, K. Pan, S. Zhang, X. Hang, M. Zheng and H. Pang, *Adv. Funct. Mater.*, 2024, **34**, 2409390.

17 Q. Liang, W. Li, L. Xie, Y. He, B. Qiu, H. Zeng, S. Zhou, J. Zeng, T. Liu, M. Yan, K. Liang, O. Terasaki, L. Jiang and B. Kong, *Nano Lett.*, 2022, **22**, 2889–2897.

18 Y. Wu, J. Liu, Q. Sun, J. Chen, X. Zhu, R. Abazari and J. Qian, *Chem. Eng. J.*, 2024, **483**, 149243.

19 A. A. Bhoite, K. V. Patil, R. S. Redekar, J. H. Jang, V. A. Sawant and N. L. Tarwal, *J. Energy Storage*, 2023, **72**, 108557.

20 R. Shokry, H. M. Abd El Salam, D. Aman, S. Mikhail, T. Zaki, W. M. A. El Rouby, A. A. Farghali, W. Al Zoubi and Y. G. Ko, *Chem. Eng. J.*, 2023, **459**, 141554.

21 S. Yu, J. Li, Y. Du, Y. Wang, Y. Zhang and Z. Wu, *Coord. Chem. Rev.*, 2024, **520**, 216144.

22 Y. Shi, B. Zhu, X. Guo, W. Li, W. Ma, X. Wu and H. Pang, *Energy Storage Mater.*, 2022, **51**, 840–872.

23 J. Guo, H. Zhao, Z. Yang, Y. Wang, X. Liu, L. Wang, Z. Zhao, A. Wang, L. Ding, H. Liu and X. Yu, *Nano Energy*, 2023, **116**, 108763.

24 Y. Hu, C. Li, S. Xi, Z. Deng, X. Liu, A. K. Cheetham and J. Wang, *Adv. Sci.*, 2021, **8**, 2003212.

25 Y. Yuan, K. Wang, B. Zhong, D. Yu, F. Ye, J. Liu, J. Dutta and P. Zhang, *Energy Environ. Mater.*, 2024, **7**, e12747.

26 H. Pan, X.-L. Wang, F. Li and Q. Xu, *J. Mater. Chem. A*, 2023, **11**, 15006–15013.

27 Z. Li, C. Xu, Z. Zhang, S. Xia, D. Li, L. Liu, P. Chen and X. Dong, *Adv. Sci.*, 2024, **11**, 2308477.

28 H. Zhang, M. Wang, B. Song, X.-L. Huang, W. Zhang, E. Zhang, Y. Cheng and K. Lu, *Angew. Chem., Int. Ed.*, 2024, **63**, e202402274.

29 M. Bi, Y. Zhang, X. Jiang, J. Sun, X. Wang, J. Zhu and Y. Fu, *Adv. Funct. Mater.*, 2024, **34**, 2309330.

30 S. Wang, M. Zhang, X. Mu, S. Liu, D. Wang and Z. Dai, *Energy Environ. Sci.*, 2024, **17**, 4847–4870.

31 U. B. Kim, D. J. Jung, H. J. Jeon, K. Rathwell and S.-G. Lee, *Chem. Rev.*, 2020, **120**, 13382–13433.

32 Y. He, S. Liu, C. Priest, Q. Shi and G. Wu, *Chem. Soc. Rev.*, 2020, **49**, 3484–3524.

33 L. Hao, T. Yu, C. Liu, J. You and R. Guo, *Energy Storage Mater.*, 2024, **72**, 103723.

34 Y. Lin, L. Yang, Y. Zhang, H. Jiang, Z. Xiao, C. Wu, G. Zhang, J. Jiang and L. Song, *Adv. Energy Mater.*, 2018, **8**, 1703623.

35 L. Wang, M. Xu, H. Li, Z. Huang, L. Wang, T. T. Isimjan and X. Yang, *Inorg. Chem.*, 2023, **62**, 13284–13292.

36 X. Li, M. Wang, H. Wang, Y. Gao, Z. Tang, J. Wang, Y. Feng, Z. Yang, D. Zhou, J. Chen, H. Xie, Y. Huang and X. Li, *ACS Appl. Mater. Interfaces*, 2022, **14**, 43215–43225.

37 S. Guo, C. Pang, P. He, X. He, J. Ren and L. Ouyang, *Appl. Surf. Sci.*, 2024, **651**, 159255.

38 J. Ma, A. Azizi, E. Zhang, H. Zhang, A. Pan and K. Lu, *Chem. Sci.*, 2024, **15**, 4581–4589.

39 H. Hu, Z. Xu, Z. Zhang, X. Yan, Y. Zhu, J. P. Attfield and M. Yang, *Angew. Chem., Int. Ed.*, 2024, **63**, e202404374.

40 H. Xia, R. Pang, X. Dong, Q. Liu, J. Chen, E. Wang and J. Li, *J. Am. Chem. Soc.*, 2023, **145**, 25695–25704.

41 P. Pachfule, D. Shinde, M. Majumder and Q. Xu, *Nat. Chem.*, 2016, **8**, 718–724.

42 Q.-D. Ruan, R. Feng, J.-J. Feng, Y.-J. Gao, L. Zhang and A.-J. Wang, *Small*, 2023, **19**, 2300136.

43 H. Tu, H. Zhang, Y. Song, P. Liu, Y. Hou, B. Xu, T. Liao, J. Guo and Z. Sun, *Adv. Sci.*, 2023, **10**, 2305194.

44 L. Wang, J. Huang, X. Hu, Z. Huang, M. Gao, D. Yao, T. T. Isimjan and X. Yang, *J. Colloid Interface Sci.*, 2024, **660**, 989–996.

45 L. Yang, C. Du, J. Tian, X. Yao, Q. Zhang, X. Ma, Y. Zhu, M. Zou and C. Cao, *Appl. Catal., B*, 2024, **355**, 124190.

46 X. Liu, W. Yan, J. Song, H. Song, W. Chen, Y. Zhang and Y. Chen, *Chem. Eng. J.*, 2024, **492**, 152301.

47 Q. Lu, X. Zou, Y. Bu, Y. Wang and Z. Shao, *Energy Storage Mater.*, 2024, **68**, 103341.

48 C. Gang, J. Chen, X. Li, B. Ma, X. Zhao and Y. Chen, *Nanoscale*, 2021, **13**, 19430–19437.

49 D. Duan, J. Huo, J. Chen, B. Chi, Z. Chen, S. Sun, Y. Zhao, H. Zhao, Z. Cui and S. Liao, *Small*, 2024, **20**, 2310491.

50 N. He, Y. Sun, X. Chen, J. Wang, G. Liang and F. Mo, *J. Mater. Chem. A*, 2024, **12**, 10101–10109.

51 S. Zhou, Q. Yang, Y. Liu, L. Cheng, T. T. Isimjan, J. Tian and X. Yang, *J. Catal.*, 2024, **433**, 115491.

52 Y. Pan, X. Ma, M. Wang, X. Yang, S. Liu, H.-C. Chen, Z. Zhuang, Y. Zhang, W.-C. Cheong, C. Zhang, X. Cao, R. Shen, Q. Xu, W. Zhu, Y. Liu, X. Wang, X. Zhang, W. Yan, J. Li, H. M. Chen, C. Chen and Y. Li, *Adv. Mater.*, 2022, **34**, 2203621.

53 W. Zhang, L. Yang, Z. Li, G. Nie, X. Cao, Z. Fang, X. Wang, S. Ramakrishna, Y. Long and L. Jiao, *Angew. Chem., Int. Ed.*, 2024, **63**, e202400888.

54 X. Hou, T. Ni, Z. Zhang, J. Zhou, S. Zhang, L. Chu, S. Dai, H. Wang and M. Huang, *Chem. Eng. J.*, 2024, **495**, 153464.

55 Z. Li, S. Ji, C. Wang, H. Liu, L. Leng, L. Du, J. Gao, M. Qiao, J. H. Horton and Y. Wang, *Adv. Mater.*, 2023, **35**, 2300905.

56 C. Fang, X. Tang and Q. Yi, *Appl. Catal., B*, 2024, **341**, 123346.

57 F. Luo, Y. Yu, X. Long, C. Li, T. Xiong and Z. Yang, *J. Colloid Interface Sci.*, 2024, **656**, 450–456.

58 L. Chai, Z. Hu, X. Wang, L. Zhang, T.-T. Li, Y. Hu, J. Pan, J. Qian and S. Huang, *Carbon*, 2021, **174**, 531–539.

59 H. Tian, L. Zeng, Y. Huang, Z. Ma, G. Meng, L. Peng, C. Chen, X. Cui and J. Shi, *Nano-Micro Lett.*, 2020, **12**, 161.